Molecular Vision 2026; 32:169-184 <http://www.molvis.org/molvis/v32/169>
Received 6 October 2025 | Accepted 1 March 2026 | Published 3 March 2026

Structural and biomechanical analysis of WST11/NIR scleral stiffening

Qian Ma,[1] Alexa Goz,[2,3] Jurriaan Brekelmans,[2,4,5] Brendan Geraghty,[6] Mor M. Dickman,[4,7] Vanessa L.S. LaPointe,[4,8] Arie L. Marcovich,[2,3] Craig Boote[1]

[1]Structural Biophysics Group, School of Optometry and Vision Sciences, Cardiff University, Cardiff, UK; [2]Department of Plants and Environmental Science, The Weizmann Institute of Science, Rehovot, Israel; [3]Department of Ophthalmology, Kaplan Medical Center, Rehovot, affiliated to the Faculty of Medicine, Hebrew University, Jerusalem, Israel; [4]University Eye Clinic Maastricht, Maastricht University Medical Center+, Maastricht, the Netherlands; [5]Department of Ophthalmology, Zuyderland Eyescan, Sittard, the Netherlands; [6]Department of Musculoskeletal and Ageing Science, Institute of Life Course and Medical Sciences, University of Liverpool, William Henry Duncan Building, Liverpool, UK; [7]Department of Ophthalmology, Division of Surgical Specialities University Medical Center Utrecht, Utrecht University, Utrecht, The Netherlands; [8]MERLN Institute for Technology-Inspired Regenerative Medicine, Maastricht University, Maastricht, the Netherlands

Purpose: To characterize structural and biomechanical changes following ex vivo treatment of rabbit sclera with the bacteriochlorophyll derivative WST11 and near-infrared (NIR) light.

Methods: Enucleated left scleras of 10 rabbits were cross-linked by a 20-min topical application of WST11 solution, followed by 30-min NIR irradiation (10 mW/cm^2). Paired right eyes served as untreated controls. Scleral tangent modulus and ultimate tensile strength were obtained from tensile strip testing. Collagen molecular-level nanostructure was measured using wide-angle X-ray scattering (WAXS). Scleral fibrillar-level microstructure was assessed using second harmonic generation (SHG) and two-photon fluorescence (TPF) imaging.

Results: WST11/NIR treatment increased scleral tangent modulus by an average of 79% for strains between 1.5% and 3% ($p < 0.05$), while ultimate tensile strength increased by 140% (control: 1.719 MPa, treated: 4.134 MPa, $p < 0.01$). WAXS indicated that collagen molecular spacing (control: 1.485 nm/treated: 1.480 nm, $p = 0.65$), spatial disorder (47.6 a.u./47.6 a.u., $p > 0.99$), and anisotropy (0.935 a.u./1.157 a.u., $p = 0.09$) were not significantly affected by treatment. No marked treatment effects on collagen fibril bundle organization were observable by SHG imaging. TPF imaging revealed additional crimped fibrous structures in the outer half of the tissue depth in treated specimens, indicative of enhanced collagen cross-linking.

Conclusions: WST11/NIR treatment significantly increased the stiffness of the ex vivo rabbit sclera. The origin of the stiffening effect is consistent with the formation of collagen cross-links that are predominantly extrafibrillar in nature. Further research is needed to establish the full mechanism, efficacy, and safety of the method as a potential myopia treatment.

The sclera is the opaque, fibrous connective tissue that, together with the transparent cornea, forms the outer tunic of the eye. Biomechanically, the sclera is well adapted to serve its primary functions of protecting the internal ocular structures, while regulating eye size and refractive status [1]. The sclera's requisite load-bearing characteristics are imparted by the specialized organization of type I fibrillar collagen—the main constituent of the stroma that accounts for about 90% of its dry weight [2]. Three polypeptide α-helix chains combine to form a single tropocollagen molecule of length ~300 nm [3]. Five parallel molecules are bonded by intermolecular cross-links in a twisted rope-like fashion to form microfibrils, where adjacent molecules are axially staggered by 67 nm [4] and tilted by 5° with respect to the microfibril axis [5]. Microfibrils are assembled as parallel arrays into fibrils [4], which, in turn, form fibrillar bundles stabilized by interfibrillar cross-links. Fibril bundles form layers (lamellae) that lie roughly parallel to the tissue surface but with degrees of interweave that vary by anatomic region [6]. Cross-link stabilization of the hierarchical collagen structure occurs by two distinct mechanisms. The first involves enzymatic cross-link formation, initiated by lysyl oxidase, that occurs during tissue assembly and maturation [3]. The second is a nonenzymatic pathway involving glycation of lysine and hydroxylysine residues, resulting in the formation of advanced glycation end-product cross-links that accumulate with age [7] and play a significant role in the observed stiffening of the aging sclera [8].

Pathological changes in the sclera occur during the development of axial myopia, including tissue thinning,

Correspondence to: Craig Boote, Cardiff University, School of Optometry and Vision Sciences, Maindy Road, Cardiff CF24 4HQ, UK; Phone: +44 (0)29 2087 0586; FAX: +44 (0)29 2087 4859; email: BooteC@Cardiff.ac.uk

viscoelastic alteration, collagen structural changes, and a reduction in collagen cross-links [9,10]. These observations have driven research into new therapeutic routes aimed at enhancing scleral mechanical properties to potentially slow or prevent myopic scleral creep. One such avenue is exogenous collagen cross-linking therapy. Delivery of chemical cross-linking agents, including glyceraldehyde [11,12] and genipin [13-16] via sub-Tenon injection, has been shown to result in stable scleral stiffening and inhibition of myopic elongation in in vivo experimental animal models. However, with such methods, it is difficult to accurately target the cross-linking agent to a specific tissue area and dose the therapy's effect. Moreover, reported complications associated with genipin include elevated intraocular pressure, a shallower anterior chamber angle, glaucomatous alterations in the optic disc, and degeneration of retinal pigment epithelium and photoreceptors [17-20]. An alternative method involves irradiation of the sclera with ultraviolet-A (UVA) light in the presence of a topically applied riboflavin photosensitizer solution [21], which has been shown to be effective in preventing axial myopia in live rabbits [22]. However, concerns remain with the potential for cytotoxic damage when exposing the retina to ultraviolet light [23]. Recently, chemical derivatives of chlorophyll and bacteriochlorophyll photosynthetic pigments have been developed that are, instead, sensitive to illumination by near-infrared (NIR) light, reducing the cytotoxic risks encountered with UVA wavelengths. We have previously demonstrated the ability of one such agent—palladium bacteriochlorin 13′-(2-sulfethyl)amidedipotassium salt (WST11)—to produce a significant and prolonged stiffening of the cornea with minimal side effects in live rabbits [24-26]. WST11 has a strong NIR-range spectral absorption peak at 755 nm [27], which has been exploited by targeted NIR light activation in clinical trials and preclinical settings, respectively, aiming to develop the modality as a photodynamic therapy for tumor ablation [27,28] and corneal cross-linking treatment [25,26]. In the current study, we report the application of this novel treatment to the sclera—assessing the structural and biomechanical effects of the treatment in ex vivo rabbit tissue, as a preliminary step toward its possible future development as a myopia therapy.

METHODS

Specimen details: Ten pairs of fresh enucleated eyes from 3-month-old New Zealand White rabbits (2.5–3.5 kg weight) were obtained from a local abattoir and transported on ice in a humid container until further processing. The left eye of each pair was used for cross-linking treatment (as detailed below), while the fellow right eye served as an untreated control. After treatment, 8-mm-diameter full-thickness scleral buttons were removed from the treatment area (and the corresponding region of controls) using a biopsy punch, wrapped in polyvinylidene chloride film, snap-frozen using liquid N_2 cooled isopentane, and stored at −80 °C for structural and biomechanical analysis. Immediately before examination, each frozen specimen was thawed/equilibrated, still film-wrapped, at room temperature for 30 min.

WST11/NIR treatment: The bacteriochlorophyll derivative WST11 was supplied by STEBA Laboratories (Rehovot, Israel). A 2.5-mg/ml solution of WST11 (pH 7.2) was prepared in saline (0.9% NaCl). Enucleated eyes were immersed for 20 min and rinsed in phosphate-buffered saline (PBS), and the same 10-mm-diameter region of the equatorial sclera (away from the extraocular muscle insertions; see Figure 1) was exposed to NIR irradiation for 30 min (10 mW/cm^2, 755 nm). The light source consisted of a diode laser with tuneable output up to 1 W at 755 nm (CeramOptec, Bonn, Germany) [26]. To prevent the sclera from drying out during irradiation, the eyes were lubricated every 5 min with PBS drops.

Tensile testing: After thawing, strips were cut in the same anatomic orientation through the center of the scleral buttons using a bespoke twin razorblade cutter with a 3-mm spacer between the blades for use in tensile tests (Figure 1). The two residual scleral pieces from each button were refrozen and stored for structural analysis (Figure 1). The scleral strips were suspended between serrated mechanical clamps surfaced with sandpaper to prevent slippage during the tests. The gauge length between the clamps was set to 6 mm. A Vernier calliper (D00352, 10-µm accuracy; Duratool, Taiwan) was used to measure the strip width at three different positions along the specimen, and the average width was calculated to be 3.737 ± 0.375 mm. The specimen thickness was measured at the same positions using an ultrasound pachymeter (Pachmate 55: 5-µm accuracy; DGH Technologies, Exton, PA), and the average thickness was calculated to be 309 ± 51 µm. The clamped specimens were placed vertically in an Instron 3366 material testing machine (Instron, Norwood, MA) equipped with a 10-N load cell (Instron 2530–428 with 0.025 N accuracy). A plastic tube, attached to the bottom clamp and filled with PBS, prevented specimen dehydration during tests [29]. A preload of 0.01 N was applied to remove any slack. A two-phase testing regimen was employed, consisting of an initial preconditioning phase of eight load/unload cycles, followed by a single load to tissue failure phase. Both phases used an elongation rate of 1.0 mm/min—as employed in previous tensile studies of the sclera by our group [29] and others [30]. Load/elongation data from phase 2 were converted to stress, σ, and strain, ε, using MS Excel (Microsoft, Redmond, WA)

and fitted using the following exponential function (Equation 1):

$$\sigma = A(e^{B\varepsilon} - 1)$$

where A and B are constants [31]. From the resulting curve, the tangent modulus, E_{tan}, was calculated as the local gradient between strains of 0.01 to 0.03, as shown in Equation 2:

$$E_{\tan} = \frac{\Delta\sigma}{\Delta\varepsilon}$$

X-ray scattering: Wide-angle X-ray scattering (WAXS) experiments were performed at the Diamond Light Source national synchrotron facility (Harwell, UK). Macromolecular crystallography beamline I02 was used in a custom-modified fiber-diffraction setup, as described previously [32,33]. An X-ray beam of wavelength 0.09795 nm was used, having an approximately square cross section of area 0.012 mm^2 at the specimen. During X-ray exposure, specimens were wrapped in polyvinylidene chloride film to prevent dehydration and mounted inside Perspex (Lucite Group Ltd, Southampton, UK) chambers with Mylar (DuPont-Teijin, Middlesborough, UK) X-ray transparent windows. The incident X-ray beam was directed perpendicular to the scleral surface, and initial specimen alignment was performed using an in-line microscope containing a central aperture to allow passage of the X-ray beam. WAXS patterns resulting from an X-ray exposure of 2 s were recorded on a Pilatus-6MF silicon pixel detector (Dectris Ltd, Baden, Switzerland) positioned 350 mm behind the specimen. For every specimen, nine discrete WAXS patterns were recorded in a 3 × 3 square grid with 0.15 mm (horizontal) × 0.15 mm (vertical) sampling intervals, with specimen translation between exposures achieved using an electronic x-y motor stage interfaced with the X-ray camera shutter. Collagen intermolecular spacing (IMS) was measured from the calibrated radial position of the circumferentially integrated equatorial peak that derives from the lateral packing dimension of tropocollagen molecules [34]. A combination of Optimas 6.5 (Media Cybernetics, Rockville, MD), Excel 2013, and Statistica 7.1 (Statsoft, Tulsa, OK) was used for data extraction, background removal, and peak measurement (Figure 2). IMS was calibrated using a WAXS pattern from powdered calcite ($CaCO_3$), which has a well-defined repeating crystal structure dimension of 0.304 nm, according to Equation 3:

$$IMS = \frac{\lambda}{\sin(\tan^{-1}\left[\frac{R_{scl}}{R_{cal}}\tan(2\sin^{-1}(\lambda / 2D_{cal}))\right])}$$

where λ is the X-ray wavelength (0.09795 nm); R_{scl} and R_{cal} are the radial pixel positions of the scleral collagen peak and calibrant peak, respectively; and D_{cal} is the first-order calibrant structure dimension (0.304 nm) giving rise to the peak at R_{cal}. To further quantify local nanostructure, for each WAXS pattern, the molecular spatial disorder was calculated from the full width at half height of the circumferentially integrated, radial WAXS peak. Additionally, the local anisotropy was computed from 1/full width at half height of the main peak of the radially integrated, circumferential WAXS pattern (i.e., the in-plane molecular orientation distribution [35]). For each specimen, the mean IMS, spatial disorder, and

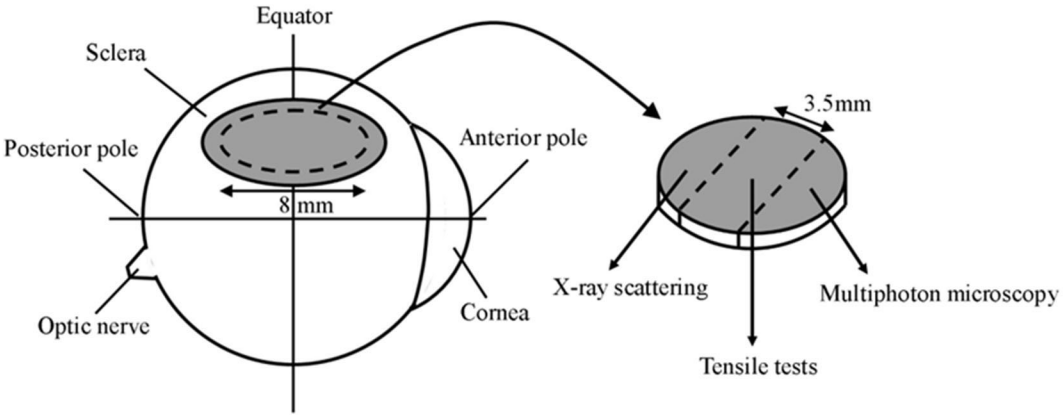

Figure 1. Location of WST11/NIR treatment area (shaded region) on the rabbit eye and the use of dissected scleral specimens. Broken lines denote dissection cuts.

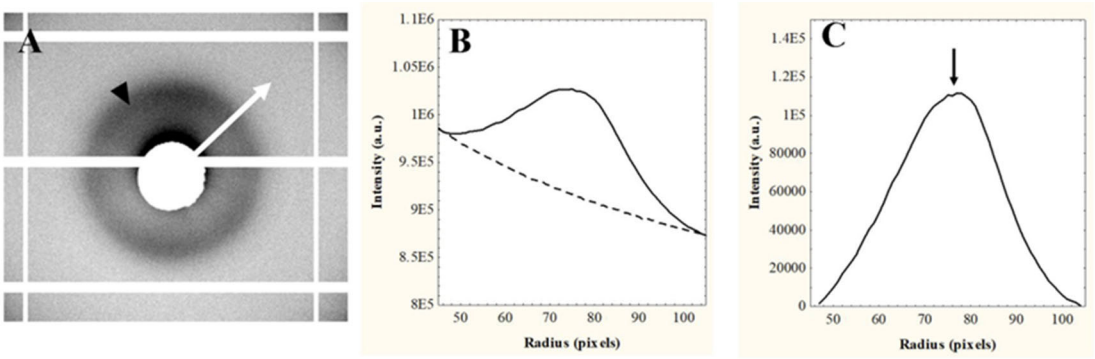

Figure 2. Wide-angle X-ray scattering (WAXS) analysis. **A**: WAXS pattern recorded from rabbit sclera. The collagen intermolecular spacing (IMS) peak (black arrowhead) is circumferentially integrated, and the radial profile is extracted along the direction of the white arrow. **B**: A power-law background function (broken line) of the form $I = aR^b$, where a and b are constants, is fitted to the extracted intensity data (solid line). **C**: Background removal allows the pixel position of the IMS peak (arrow) to be measured.

anisotropy values of the nine discrete WAXS sampling points were used in a subsequent statistical analysis.

Multiphoton imaging: For multiphoton imaging, full-thickness scleral specimens (~300 µm thick) were slide-mounted in 1:1 PBS/glycerol to maintain tissue hydration and minimize refractive index mismatching [36]. Nonlinear laser scanning multiphoton microscopy was performed using a Zeiss LSM 880 META NLO microscope (Carl Zeiss Ltd, Welwyn Garden City, UK). Second harmonic generation (SHG) signals from fibrous collagen were generated using an ultrafast titanium-sapphire tuneable infrared (680–1080 nm) laser (Cameleon Vision II; Coherent, Inc., Ely, UK) operating at 800 nm (140-fs pulse duration, 80-MHz repetition rate) and detected in the forward scattered direction after passing through a 400-nm (bandwidth 6 nm) filter matched to the spectral peak of collagen [37]. In addition, back-scattered two-photon fluorescence (TPF) signals were generated in a second channel using a bandpass filter centered on 505 nm with a bandwidth of 119 nm, matching the spectral peak of elastin [37,38]. For both SHG and TPF imaging, a 425 × 425-µm field of view with an x-y resolution of 4.8 pixels/µm was obtained using a 20× 1.0 N.A. Differential interference contrast (DIC; D = 0.17) water immersion objective lens (W Plan-Apochromat; Carl Zeiss Ltd). A 5 × 5 field-of-view tiling, covering, in total, a 3.84-mm^2 area of the treatment region, was obtained using motorized x-y stages. Eight-bit images were recorded with non-descanned NDD2 (for SHG, Carl Zeiss Ltd) and BIG2 (for TPF, Carl Zeiss Ltd) detectors. Optical sections through the full-thickness tissue were obtained at z-intervals of 25 µm. Ramped laser power correction (1.5%–7.5% of maximum) was used to compensate for increasing attenuation of the signal at deeper tissue depths.

For quantification of observed changes in TPF signal appearance due to WST11/NIR treatment, TPF images were processed using custom-developed MATLAB (MathWorks, Natick, MA) code. For selected tissue depths of each specimen, 13 discrete 500 × 500-pixel regions were randomly selected. The raw image file of each region (Figure 3A) was individually smoothed with a 0.6 SD Gaussian noise filter and manually thresholded using a semi-adaptive approach to remove background noise and produce a binary mask of pixels representing the isolated TPF signal (Figure 3B). Segmentation and quantification of the TPF signal were done using an adaptation of the protocol described by Raub and Suresh [39]. In brief, low-end threshold values (in the range 70–160 of 255) were selected for each region individually by progressively increasing the value until just before fibrous structures began to be lost (i.e., maintaining fiber morphology as close as possible to the raw images). The binary mask of selected pixels was then applied to the original image pixel intensities to generate the thresholded image (Figure 3C) for subsequent numerical analyses in MATLAB. To minimize potential batch-to-batch variability, all TPF measurements were performed on samples processed in a single batch, on the same day, and by a single operator (QM) blinded to the sample groups. To assess TPF measurement repeatability, 18 independent images were selected. A single operator (QM) performed five repeated measurements on each image. For each image, the mean, standard deviation, and coefficient of variation were calculated. The coefficient of variation values ranged from 3.9% to 19.3%, indicating generally low measurement variability, with a one-way intraclass correlation coefficient (ICC) of 0.997 (95% confidence interval, 0.992–0.999). Two parameters were computed: (1) the TPF image fraction, defined as the number of segmented pixels

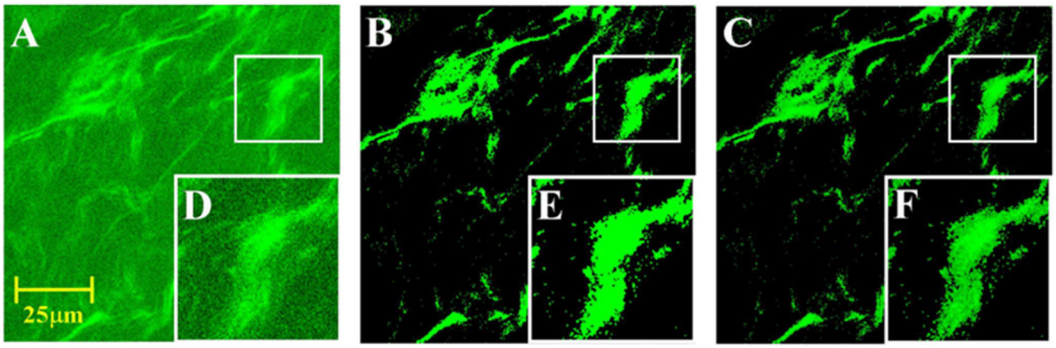

Figure 3. Two-photon fluorescence (TPF) image processing. **A**: Raw TPF image. **B**: Binary mask of noise-filtered and thresholded pixels to isolate TPF-emitting structures. **C**: Mask from (**B**) is applied to raw image in (**A**) to produce the final segmented image for numerical analysis. **D–F**: Region of interest bounded by white squares is shown at 4× magnification.

expressed as a percentage of the total image pixels, and (2) the total TPF signal, defined as the summed value of segmented pixels. Mean parameters for the 13 regions were obtained for each specimen and compared between control and treated groups individually at superficial (50 µm), mid (150 µm), and deep (300 µm) tissue depths.

Statistical analysis: Pairwise comparison of WAXS and TPF data between control and WST11/NIR-treated specimens was performed using the software package Statistica 7.1 (Statsoft, Tulsa, OK). Normality of datasets was established using the Shapiro-Wilk test. All datasets were found to have a normal distribution ($p > 0.120$, $W > 0.876$), with the exception of TPF controls at a 300-µm depth ($p = 0.025$, $p = 0.0036$; $W = 0.819$, $W = 0.750$). For comparisons involving these nonparametric data, Wilcoxon signed-rank tests were used, while for the remainder of the (parametric) data, two-tailed paired *t* tests were employed. Tensile data statistical analysis was performed in Python (version 3.10) using a mixed-effects model with treatment and strain as fixed effects, with their interaction included, and animal as a random effect. Post hoc paired *t* tests were performed to compare control and treated eyes at each strain. Multiple comparisons across strain points were controlled using the Holm-Bonferroni method. Effect sizes (Cohen's *d*) with 95% confidence intervals and post hoc statistical power were also calculated.

RESULTS

Tensile testing: All scleral strip specimens displayed nonlinear tensile behavior with an initial low stiffness response that increased exponentially as a function of strain. Group-averaged stress–strain results are shown in Figure 4A, while corresponding plots of tangent modulus versus strain are displayed in Figure 4B. As shown in Table 1, WST11/NIR treatment, on average, resulted in statistically significant increases in stiffness (E_{tan}) of 89% ($p = 0.042$), 82% ($p = 0.015$), and 68% ($p = 0.001$) at strains of 1.5%, 2%, and 3%, respectively, while the 95% increase at 1% strain fell below the significance threshold ($p = 0.091$). Treatment also increased the ultimate breaking stress by 140% ($p = 0.004$), from 1.719 MPa (control average) to 4.134 MPa (treated average).

X-ray scattering: During WAXS experiments, all scleral specimens yielded an equatorial (i.e., perpendicular to the fibril long axis) X-ray scatter peak that indexed on 1.44 to 1.52 nm, consistent with the lateral spacing of individual tropocollagen molecules that make up scleral fibrils [2,36,40]. Calibrated values of average (n = 9 sampled points) intermolecular Bragg spacing for the 10 individual control/treated paired samples are shown in Figure 5A. As shown in Figure 5B, group mean Bragg spacing was not statistically different between control (IMS = 1.480 nm) and treated (IMS = 1.484 nm) specimens ($p = 0.65$). As shown in Figure 6, molecular spatial disorder (47.6 a.u./47.6 a.u., $p > 0.99$) and anisotropy (0.935 a.u./1.157 a.u., $p = 0.09$) were also not significantly affected by the treatment, while reference to Figure 7 indicates no marked treatment changes in the (essentially random) in-plane molecular orientation distribution of the rabbit scleral specimens.

Multiphoton imaging: Representative images of SHG signals recorded from the superficial (50 µm depth), mid (150 µm), and deep (300 µm) stroma of the rabbit sclera are shown in Figure 8. Densely packed, crimped fibrous structures representing the collagen fibril bundle architecture were visible throughout the stromal depth in all specimens. SHG imaging did not reveal any noticeable changes in the collagen microstructure as a result of WST11/NIR treatment (Figure 8).

Figure 9 presents the results of TPF imaging. Fluorescence signal from a branched network of fine, straight

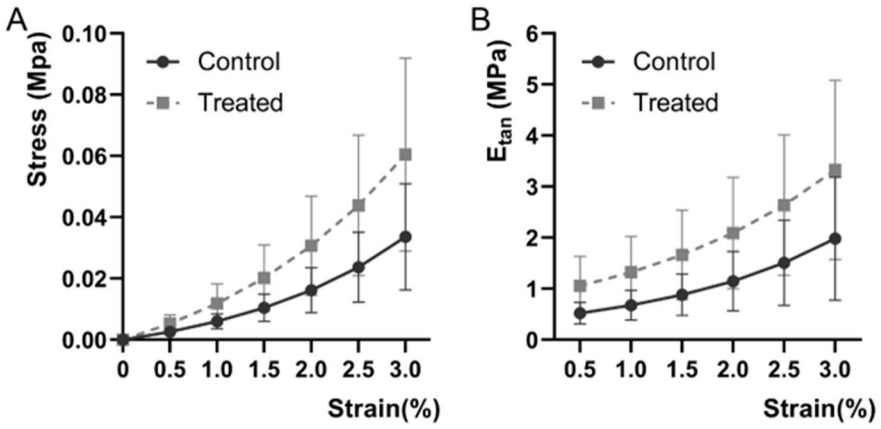

Figure 4. Tensile test results. **A**: Group-averaged stress versus strain behavior of control (solid line) and WST11/NIR treated (broken line) rabbit scleral strips. **B**: Corresponding values of tangent modulus (E_{tan}) as a function of strain. Error bars denote standard deviation.

Table 1. Tensile testing results.

Strain (%)	E_{tan} (MPa)		ΔE_{tan}	p-value	Effect size (Cohen d)	95% CI	Post hoc power
	Control	Treated					
0.5	0.525	1.056	+101%	0.1631	1.31	−1.283 ~0.220	0.91
1.0	0.678	1.324	+95%	0.0911	1.28	−1.397 ~0.106	0.90
1.5	0.881	1.663	+89%	0.0417	1.22	−1.533 ~0.030	0.88
2.0	1.150	2.092	+82%	0.0147	1.15	−1.694 ~-0.190	0.85
2.5	1.507	2.636	+75%	0.0037	1.06	−1.880 ~-0.377	0.80
3.0	1.984	3.327	+68%	0.0006	0.96	−2.095 ~-0.592	0.74

Group averaged tangent modulus (E_{tan}) of control and WST11/NIR-treated rabbit scleral strips at strains between 0.5% and 3%. ΔE_{tan} denotes percentage change due to treatment.

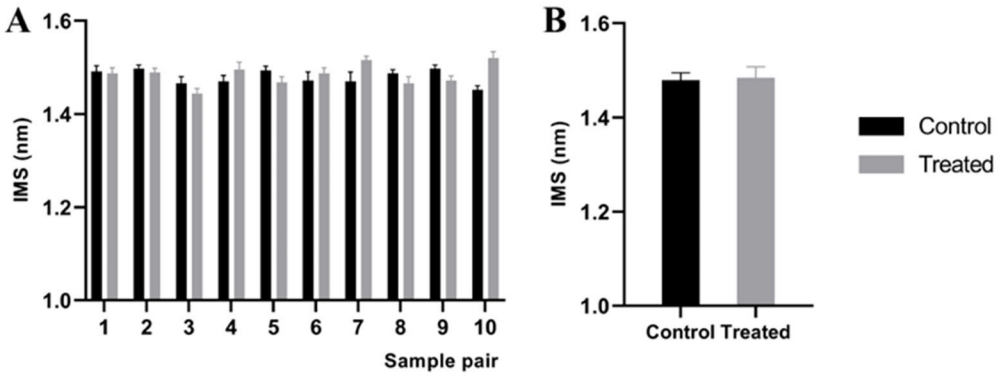

Figure 5. X-ray scattering results. **A**: Collagen intermolecular spacing (IMS) for individual pairs of control and WST11/NIR-treated rabbit scleral specimens, as determined using wide-angle X-ray scattering (WAXS). **B**: Group-averaged means of the data shown in (A). Error bars denote standard deviation.

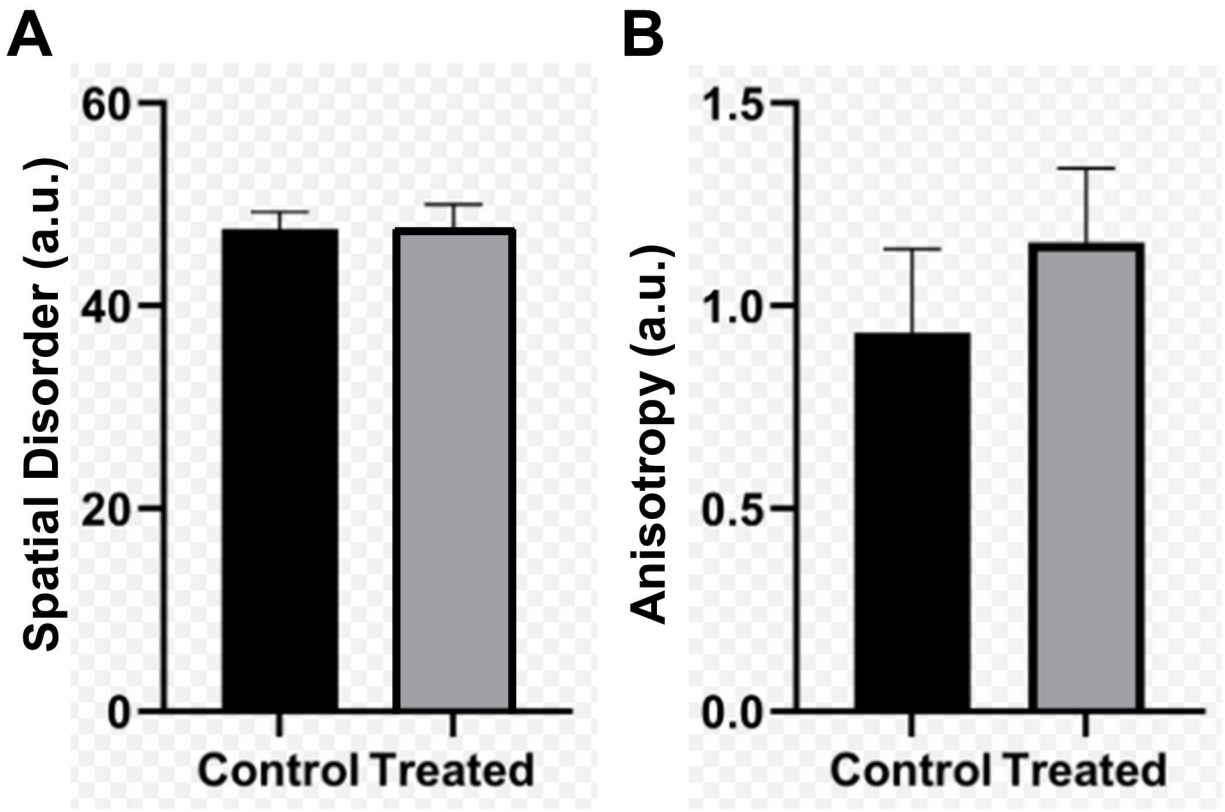

Figure 6. X-ray scattering results. **A**: Scleral collagen molecular spatial disorder, as determined using the full width at half maximum (FWHM) of the radial WAXS peak. **B**: Scleral collagen molecular anisotropy, as determined using the 1/FWHM of the principal circumferential wide-angle X-ray scattering (WAXS) peak. Values are presented as means of control and WST11/NIR treatment groups. Error bars denote standard deviation.

filaments was visible in all specimens (Figure 9A–F; single arrowheads), and this network became notably denser in the deeper tissue (Figure 9C, F). Furthermore, in the superficial half of the stroma, WST11/NIR-treated specimens exhibited fluorescent structures that were notably thicker, brighter, and wavier than the aforementioned filaments (Figure 9D, E; double arrowheads). Detection of these additional structures was enhanced by quantifying the noise-filtered and thresholded TPF signal (Figure 9G–L). This revealed that the image fraction of the segmented TPF signal was significantly increased as a result of WST11/NIR treatment by sevenfold in the superficial stroma (control = 1.2%; treated = 8.6%; $p < 0.001$; Figure 9G) and twofold in the mid-stroma (control = 3.2%; treated = 6.4%; $p < 0.001$; Figure 9H). Quantification of the total TPF signal showed proportional increases in the superficial (control = 0.53 a.u.; treated = 3.68 a.u.; $p < 0.001$; Figure 9J) and mid-depth (control = 1.26 a.u.; treated = 2.17 a.u.; $p < 0.01$; Figure 9K) tissue. TPF image fraction (control = 7.9%; treated = 6.3%; Figure 9I) and total signal (control = 3.67; treated = 2.58; Figure 9L) in the deep stroma were marginally decreased by WST11/NIR treatment, but these differences were not statistically significant ($p > 0.05$).

DISCUSSION

This study has examined the biomechanical and structural effects of WST11/NIR treatment on the sclera. We have demonstrated that the treatment can significantly increase scleral stiffness ex vivo in rabbit tissue, marking it as a potential therapeutic route to slowing or arresting myopic axial elongation. Moreover, we used a combination of imaging and scattering methods to study the structural effects of the treatment on the scleral extracellular matrix at microstructural (i.e., extrafibrillar) and nanostructural (intrafibrillar) resolutions, noting from TPF imaging a marked alteration of the sclera's fibrous tissue morphology in the outer half of the stroma. Taken as a whole, the structural data point predominantly to an enhancement of extrafibrillar collagen crosslinks and are compatible with the corresponding increases

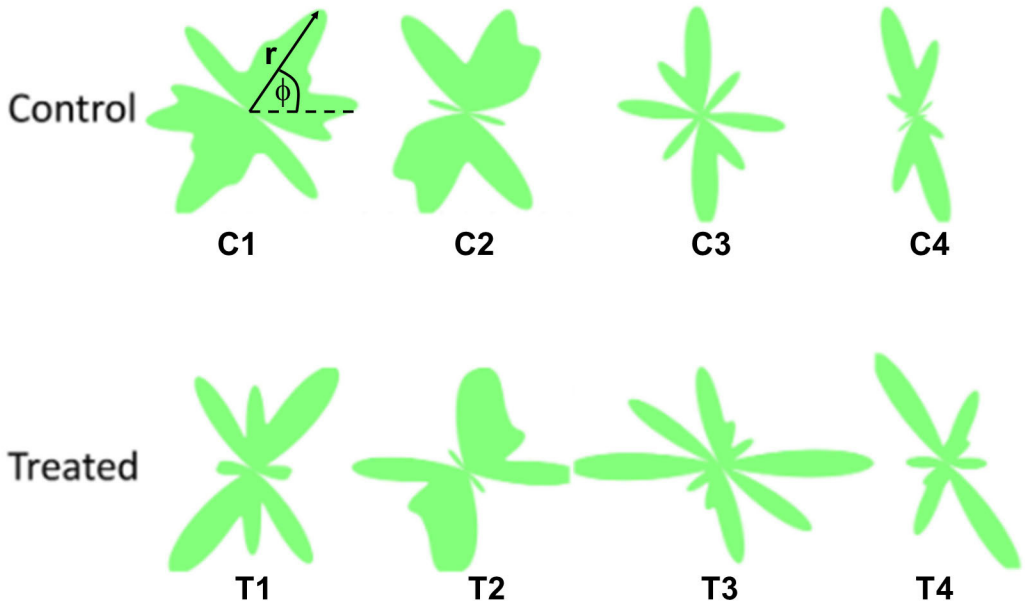

Figure 7. X-ray scattering results. Polar vector plots of scleral collagen orientation distribution for four control/treatment sample pairs, as determined using wide-angle X-ray scattering (WAXS). For each plot, the length of vector **r** represents the relative number of collagen molecules aligned at angle ϕ within the scleral plane, as an average through the tissue thickness.

in both scleral tensile stiffness and ultimate breaking stress documented herein.

Multiphoton microscopy has been extensively used to image extracellular matrix microstructure in the sclera [36,41-47] and other connective tissues [37-39,48-53]. TPF signal recorded in the spectral region of 505 nm has been widely shown to register with elastin [37,38,48-50], a major component of mature elastic fibers [54]. Accordingly, we have used TPF here to visualize the elastic fiber system of the rabbit sclera, visible in all specimens as a branched network of straight fibers (Figure 9A–F). This network became visibly denser in the deep sclera (Figure 9C, F). While the depth-wise distribution of elastin/elastic fibers in the sclera is not well characterized, studies in human [49,55,56] and mouse [57] corneas have identified an elastic fiber network in the limbal region that is located in the posterior stroma just above Descemet's membrane and appears continuous with the neighboring deep scleral tissue [55-57]. We hypothesize that the increase in density of the elastic fiber network in the deep scleral stroma identified herein reflects elastic structures that are continuous with the limbal elastic network.

The most striking result of the TPF imaging was the presence, in WST11/NIR-treated specimens, of additional thick, wavy fibrous structures (Figure 9D, E) that contrasted markedly in morphology from the aforementioned branched network of thinner, straighter fibers identified with elastin. These resulted in a significant elevation of the TPF signal (Figure 9G, H, J, K). Our contention is that this additional signal originates from treatment-induced collagen cross-links, which appear closely similar to short sections of crimped collagen fibril bundles revealed by SHG (see TPF/SHG signal overlay in Figure 10). In further support of this argument, a growing body of literature correlates the recorded TPF signal with the presence of cross-link fluorophores [39,51,52,58]. Moreover, other collagen cross-linking treatments have been shown to result in a similar enhancement of the TPF signal. Specifically, Raub and Suresh [39] reported a significant threefold increase in segmented TPF signal in collagen hydrogel scaffolds after glutaraldehyde cross-linking, while Steven and coworkers [51] demonstrated an increase in corneal cross-links from fluorescence signal measurements following riboflavin/UVA collagen cross-linking in live rabbits. Importantly, previous photodynamic studies performed by our group [26] have established the fundamental mechanism of corneal stiffening by NIR light-activated WST11 to be based on the generation of hydroxyl and superoxide radicals, without singlet oxygen, consistent with a role in the promotion of protein cross-linking [59]. Taken together with the close compositional similarity between the cornea and sclera [1,60], this further supports our hypothesis that enhanced collagen cross-linking is a

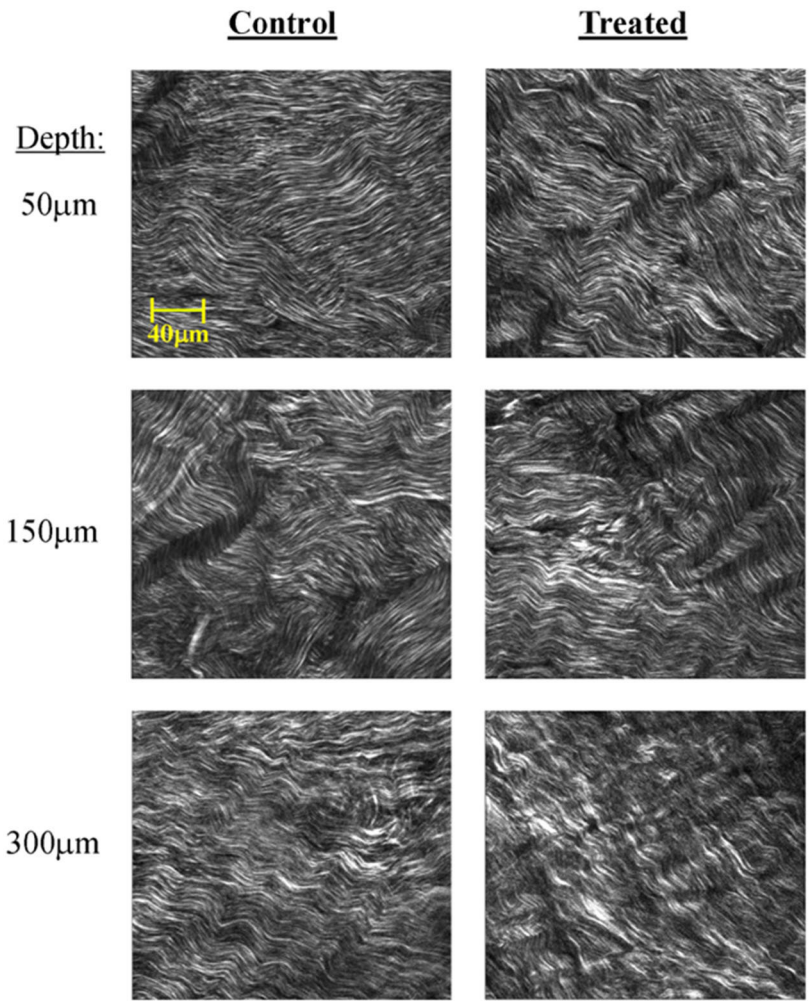

Figure 8. Second harmonic generation (SHG) imaging results. Representative SHG images from control and WST11/NIR- treated rabbit scleral specimens recorded from superficial (50 μm), mid (150 μm), and deep (300 μm) stroma. Crimped collagen fibril bundle architecture does not display any marked differences between control and treatment groups.

key underlying feature of scleral stiffening by WST11/NIR treatment. The enhancement in the TPF signal observed in the current study was most pronounced in the superficial tissue and regressed by the mid-stroma, suggesting that the treatment only affected the outer half of the sclera. This is likely due to the limited penetration of the photosensitizer solution, as noted in our previous study of WST11/NIR treatment in the rabbit cornea [26]. The current observation of a marginal (nonsignificant) decrease in the TPF signal in the deep sclera as a result of treatment (Figure 9I, L) may be because the treatment results in a green staining of the tissue that may have caused some additional attenuation of the emitted (back-scattered) signal in the treated specimens compared to controls. This effect would have been swamped in the more superficial tissue by the proportionally greater increase in TPF signal due to the induced presumptive cross-link fluorescence.

The type and location of cross-links formed by exogenous treatments are important, given that these factors are known to affect collagen catabolism [61-63], and hence may impact the longevity of any induced therapeutic stiffening at the tissue level. To investigate the nature (intra- or extrafibrillar) of the potential collagen cross-links induced by WST11/NIR treatment, we first applied WAXS to detect any intrafibrillar changes in collagen structure. A marked increase in intrafibrillar cross-links would manifest as an elevation of collagen IMS, detectable by WAXS, as the cross-links push the molecules apart. Such a scheme has been demonstrated previously by the same technique in studies of corneoscleral and tendon collagen as a function

of age [40], in vitro glycation [64-66], and glutaraldehyde cross-linking [67]. In the present study, we did not find any measurable alteration in the collagen molecular spacing (Figure 5), suggesting that no widespread, transverse cross-linking between neighboring molecules occurred as a result of WST11/NIR treatment. This conclusion is strengthened by the concurrent lack of alteration in molecular spatial disorder, as reported herein (Figure 6). Moreover, a lack of nanoscale changes with treatment is further consistent with the findings from Hayes et al. [64], where WST11/NIR cross-linked rabbit corneas exhibited no differences in IMS, as also measured by WAXS, compared to untreated corneas. As such, the mechanism of WST11/NIR stiffening appears to contrast with that of the glycation-induced aging pathway in being evidently predominantly extrafibrillar in nature. Of interest, a lack of molecular structure alteration has also been reported in WAXS studies of corneal riboflavin/UVA cross-linking [68]. However, as also noted in that study, the possibility of cross-links forming within and/or between collagen molecules situated at the fibril surface cannot be ruled out, as that scenario would be expected to result in more subtle changes to molecular packing that may be unmeasurable by WAXS due to both the averaging nature of the technique and its inherent detection limit (~1 pm) [68]. Moreover, since the X-rays were directed at the specimen en face, the values of collagen molecular spacing obtained from WAXS are an average of the full tissue thickness and therefore include a contribution from the unmodified deeper stroma, where the treatment did not penetrate. With these factors in mind, future work is warranted to probe scleral nanostructure as a function of tissue depth, which could exploit, for example, recent advances in synchrotron micro-focus WAXS technology capable of examining ocular tissue strips edge-on [69]. It should also be considered that our proposal of extrafibrillar cross-linking is a plausible, but not unique, explanation for the observed lack of IMS change. An alternative explanation involves the formation of nontransverse, intrafibrillar cross-linking between telopeptide regions that may enhance tensile stiffness of collagen tissues without manifesting in an increase in IMS [70]. While we did not detect any other nanoscale changes in molecular order or anisotropy that might support such a scenario, it cannot be currently ruled

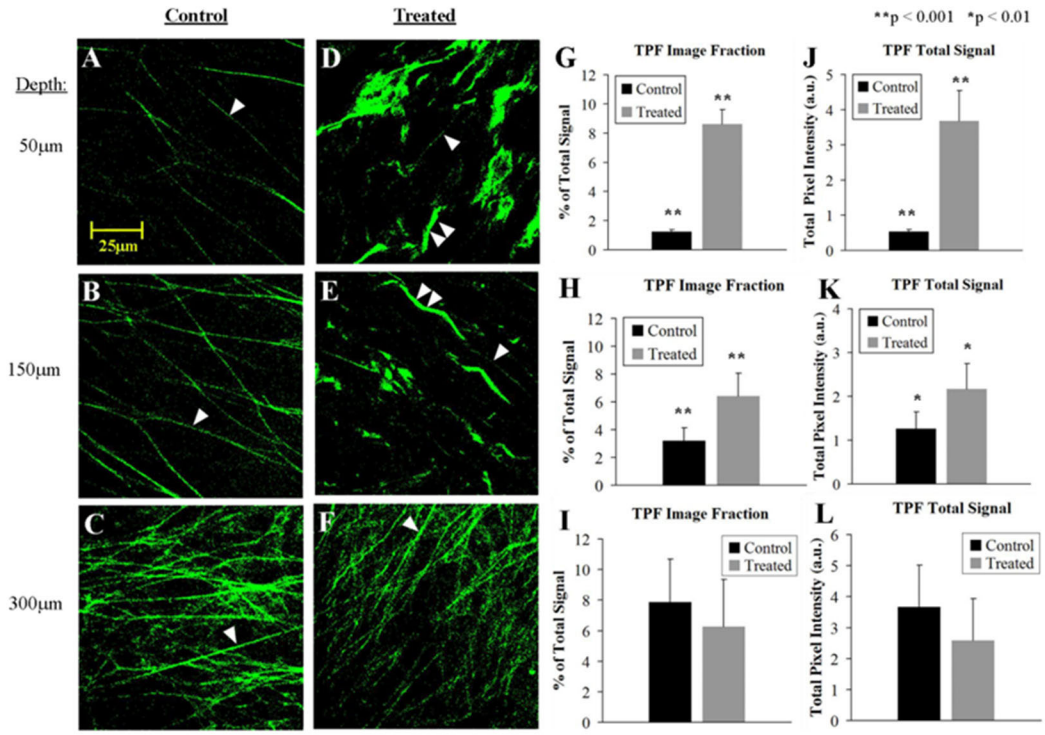

Figure 9. Two-photon fluorescence (TPF) imaging results. **A**–**F**: Noise-thresholded TPF images from control (**A**–**C**) and WST11/NIR-treated (**D**–**F**) rabbit sclera specimens at superficial (**A**, **D**), mid (**B**, **E**), and deep (**C**, **F**) tissue depths. Single arrowheads: a branched network of thin, straight fibers is observed throughout the stroma in all specimens. Double arrowheads: additional thicker and wavier fibrous structures are visible in the superficial and mid-stromal depths of WST11/NIR-treated specimens only. **G–I**: TPF image fraction is significantly increased in the superficial and mid-stroma but is marginally and nonsignificantly reduced in the deep stroma. **J–L**: A corresponding trend is also observed for total (summed) segmented TPF signal. Error bars denote standard deviation.

out. A further experimental limitation of the current study relates to our use of frozen/thawed tissue. Collagen tissues subjected to freeze/thawing are subject to potential biomechanical changes deriving from alteration in hydration, crimp status, and, moreover, the formation of directional ice crystals that may alter collagen fibril-associated ion concentrations and glycosaminoglycan interactions [71]. To mitigate this potential bias in our tensile data, we employed snap-freezing to reduce crystalline ice formation and ensured standardized thaw/equilibration times for all specimens.

To assess the connective tissue microstructure for extrafibrillar effects, we employed SHG multiphoton imaging. SHG signals excited by incident wavelengths ≥800 nm originate exclusively from the collagen fibril bundle architecture [36,41,43-46,53]. Notably, Zyablitskaya et al. [46,72] investigated the effect of in vivo sodium hydroxymethylglycinate cross-linking on scleral collagen microstructure in rabbits by SHG imaging, reporting a significant straightening of the crimped fibril bundle architecture. Compatible with this, Steven and coworkers [49] also noted a marked loss of tissue "folds" or "undulations" using SHG following riboflavin/UVA corneal cross-linking in live rabbits. In contrast, we did not observe any such changes to the collagen fibril bundle architecture as a result of WST11/NIR treatment (Figure 8). Importantly, the studies by Zyablitskaya and Steven describe cross-linking in live rabbits (i.e., with the eye under pressure), whereas the present study involved ex vivo treatment of enucleated tissue. It is known that the presence and level of intraocular pressure are important determinants of collagen crimp period [73] and its possible alteration by exogenous cross-linking [74,75]. Thus, as noted by Zyablitskaya [44], it is possible that cross-link–induced straightening of collagen observed by themselves and Steven et al. resulted from the treatment "fixing" the tissue in a mechanically loaded (i.e., straightened) position, whereas, in contrast, the untreated tissue relaxed (and became crimped) on enucleation/dissection. In our study, such an effect would not occur since the tissue was already in a relaxed state during treatment. Similarly, Bueno and coworkers [76] used SHG to interpret ex vivo cross-linking in enucleated bovine and porcine corneas, also reporting no change in collagen crimp and instead noting an increased randomization of the collagen directions with localized bundle thickening. However, this may have resulted from dehydration of the tissue due to riboflavin-dextran instillation, rather than the cross-linking process itself [76]. While we did not note any clear alteration in the collagen fibril bundle microstructure in the present study, it should be emphasized that SHG imaging cannot resolve structure at the level of individual collagen fibrils but rather visualizes fibrillar bundle structures. Further studies of WST11/NIR treatment in sclera are warranted that include structural techniques with single-fibril resolution, such as atomic force microscopy [77] and transmission electron microscopy [78]. Moreover, additional photodynamic investigations of WST11 are warranted under conditions aligned with the current study. Such studies may help to shed further light on the potential formation and type of extrafibrillar cross-links induced by WST11/NIR treatment, with a range of possible

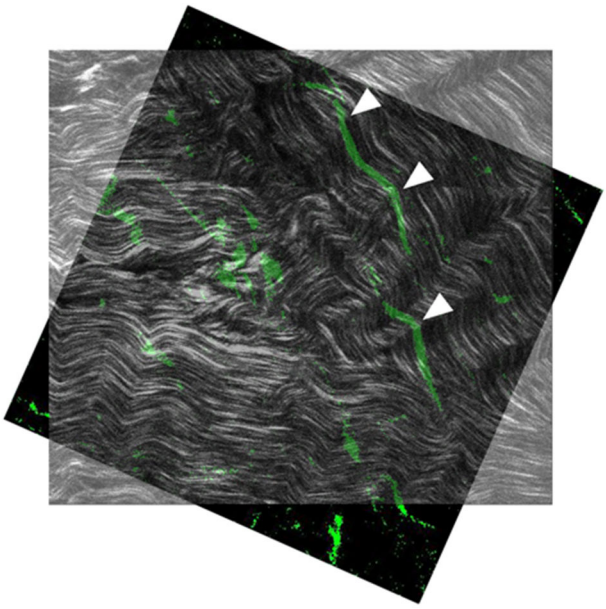

Figure 10. Overlay of two-photon fluorescence (TPF) and second harmonic generation (SHG) images of sclera in the WST11/NIR-treated group at a depth of 50 µm. Arrowheads: similar crimped morphology between the treatment-induced wavy structures in TPF and the collagen in SHG.

scenarios that include fibril–fibril, fibril–proteoglycan, and proteoglycan–proteoglycan interactions [68].

The potential clinical benefit of scleral stiffening by WST11/NIR treatment currently remains theoretical. As mentioned, other scleral cross-linking strategies targeting the posterior sclera have already been shown to be effective in attenuating axial elongation and/or scleral softening in animal models [12,14]. In the current study, we targeted the equatorial sclera for treatment. This rationale is based on emerging recent evidence from experimental animal myopia models that it is the equatorial region, rather than the posterior tissue, that is subject to the highest degree of softening in early stages of myopic axial lengthening [79,80]. Exactly how much WST11/NIR scleral stiffening would be required to effectively attenuate axial elongation also awaits validation through further in vivo experiments. However, as an indicator, previous studies in rabbits using glyceraldehyde cross-linking demonstrated significant attenuation of lens-induced myopic axial elongation resulting from a treatment-induced increase in scleral Young's modulus of 76% [12] (i.e., comparable to the degree of stiffening achieved with WST/NIR treatment in the current study). Clinical translation of the current work would also rely on safety concerns being fully met. Toward this, we have previously characterized the exposure tolerance of the rabbit retina to a 755-nm NIR light exposure. In brief, in vivo transpupillary NIR exposure (755 nm, 50 mW/cm^2, 10 min; i.e., in excess of the total dose used in the current study) was applied without WST11 administration. Retinal structure and function were assessed using optical coherence tomography, electroretinogram, and histologic examination. The results showed that retinal layer thickness remained stable, electroretinogram a- and b-wave amplitudes exhibited no significant changes, and histology revealed no necrosis, inflammation, or structural abnormalities [81]. Choroidal NIR exposure tolerance is a further important safety consideration, as well as the potential for cytotoxic risk of the WST11 solution to the choroid, retina, and adjacent tissues (e.g., optic nerve). These aspects will require validation in future work. In terms of potential clinical translation, the penetrating nature of NIR light opens the potential for transpupillary light delivery. We have previously demonstrated feasibility in ex vivo rabbit eyes, where a twofold increase in equatorial scleral Young's modulus was achieved by transpupillary NIR exposure in combination with topical WST11 application [81], and we are currently exploring this capability in enucleated human eyes. Moreover, our preliminary work has established that in vivo delivery of the WST11 solution can be administered via cannula to the sub-Tenon's space, with subsequent diffusion to the equatorial and posterior sclera achievable in rabbits [81] and guinea pigs [82]. Further studies are needed to establish detailed parameters for any clinically deliverable treatment.

In conclusion, the present study has shown that WST11/NIR treatment can significantly increase the stiffness of the ex vivo rabbit sclera and that the origin of this stiffening effect is consistent with the formation of collagen cross-links that are predominantly extrafibrillar in nature. Further in vivo experiments are needed to establish the full mechanism, efficacy, and safety of the method as a potential myopia treatment.

ACKNOWLEDGMENTS

The authors thank Tessa Antonisse, Jacek Pijanka, Johanna Sprangers, Petar Markov, Ashkan Eliasy, Vision Sciences Bioimaging Labs (Cardiff University, UK), and staff at the Diamond Light Source (Harwell, UK) for advice and technical contributions. Access to Diamond MX beamlines is gratefully acknowledged under proposals MX31430 and MX36304. This work was supported by National Institutes of Health grant RO1EY021500 (sub-award: 2003284605), a China Scholarship Council PhD studentship award and the Dutch Research Council (NWO, Veni).

REFERENCES

1. Boote C, Sigal IA, Grytz R, Hua Y, Nguyen TD, Girard MJA. Scleral structure and biomechanics. Prog Retin Eye Res 2020; 74:100773[PMID: 31412277].
2. Meek KM. The Cornea and Sclera. In: Fratzl P, editor. Collagen: Structure and Mechanics. Boston, MA: Springer US; 2008. p. 359–96.
3. Bailey AJ, Paul RG, Knott L. Mechanisms of maturation and ageing of collagen. Mech Ageing Dev 1998; 106:1-56. [PMID: 9883973].
4. Piez KA, Miller A. The structure of collagen fibrils. J Supramol Struct 1974; 2:121-37. [PMID: 4437176].
5. Yamamoto S, Hashizume H, Hitomi J, Shigeno M, Sawaguchi S, Abe H, Ushiki T. The subfibrillar arrangement of corneal and scleral collagen fibrils as revealed by scanning electron and atomic force microscopy. Arch Histol Cytol 2000; 63:127-35. [PMID: 10885449].
6. Komai Y, Ushiki T. The three-dimensional organization of collagen fibrils in the human cornea and sclera. Invest Ophthalmol Vis Sci 1991; 32:2244-58. [PMID: 2071337].
7. Bailey AJ. Molecular mechanisms of ageing in connective tissues. Mech Ageing Dev 2001; 122:735-55. [PMID: 11322995].
8. Schultz DS, Lotz JC, Lee SM, Trinidad ML, Stewart JM. Structural factors that mediate scleral stiffness. Invest Ophthalmol Vis Sci 2008; 49:4232-6. [PMID: 18539943].

9. Grytz R, Siegwart JT Jr. Changing material properties of the tree shrew sclera during minus lens compensation and recovery. Invest Ophthalmol Vis Sci 2015; 56:2065-78. [PMID: 25736788].

10. Vurgese S, Panda-Jonas S, Jonas JB. Scleral thickness in human eyes. PLoS One 2012; 7:e29692[PMID: 22238635].

11. Wollensak G, Iomdina E. Long-term biomechanical properties after collagen crosslinking of sclera using glyceraldehyde. Acta Ophthalmol 2008; 86:887-93. [PMID: 18537936].

12. Lin X, Naidu RK, Dai J, Zhou X, Qu X, Zhou H. Scleral Cross-Linking Using Glyceraldehyde for the Prevention of Axial Elongation in the Rabbit: Blocked Axial Elongation and Altered Scleral Microstructure. Curr Eye Res 2019; 44:162-71. [PMID: 30222005].

13. Liu TX, Wang Z. Biomechanics of sclera crosslinked using genipin in rabbit. Int J Ophthalmol 2017; 10:355-60. [PMID: 28393024].

14. Levy AM, Fazio MA, Grytz R. Experimental myopia increases and scleral crosslinking using genipin inhibits cyclic softening in the tree shrew sclera. Ophthalmic Physiol Opt 2018; 38:246-56. [PMID: 29691925].

15. Hannon BG, Luna C, Feola AJ, Ritch MD, Read AT, Stinnett SS, Vo H, Pardue MT, Gonzalez P, Ethier CR. Assessment of Visual and Retinal Function Following In Vivo Genipin-Induced Scleral Crosslinking. Transl Vis Sci Technol 2020; 9:8-[PMID: 32974080].

16. Hannon BG, Schwaner SA, Boazak EM, Gerberich BG, Winger EJ, Prausnitz MR, Ethier CR. Sustained scleral stiffening in rats after a single genipin treatment. J R Soc Interface 2019; 16:20190427[PMID: 31615330].

17. Hamdaoui ME, Levy AM, Stuber AB, Girkin CA, Kraft TW, Samuels BC, Grytz R. Scleral crosslinking using genipin can compromise retinal structure and function in tree shrews. Exp Eye Res 2022; 219:109039[PMID: 35339475].

18. Guo L, Hua R, Zhang X, Yan TY, Tong Y, Zhao X, Chen SC, Wang M, Bressler NM, Kong J. Scleral Cross-Linking in Form-Deprivation Myopic Guinea Pig Eyes Leads to Glaucomatous Changes. Invest Ophthalmol Vis Sci 2022; 63:24-[PMID: 35594036].

19. El Hamdaoui M, Levy AM, Gaonkar M, Gawne TJ, Girkin CA, Samuels BC, Grytz R. Effect of Scleral Crosslinking Using Multiple Doses of Genipin on Experimental Progressive Myopia in Tree Shrews. Transl Vis Sci Technol 2021; 10:1-[PMID: 34003978].

20. Guo Z, Wei Z, Tong Y, Chen S, Zhao X, Ma B, Guo L, Fan L. Efficacy and Safety Evaluation of Scleral Cross-Linking Using Genipin in the Treatment of Juvenile Guinea Pigs with High Myopia. J Ocul Pharmacol Ther 2023; 39:643-52. [PMID: 37582278].

21. Wollensak G, Iomdina E. Long-term biomechanical properties of rabbit cornea after photodynamic collagen crosslinking. Acta Ophthalmol 2009; 87:48-51. [PMID: 18547280].

22. Dotan A, Kremer I, Gal-Or O, Livnat T, Zigler A, Bourla D, Weinberger D. Scleral Cross-linking Using Riboflavin and Ultraviolet-A Radiation for Prevention of Axial Myopia in a Rabbit Model. J Vis Exp 2016; 110e53201[PMID: 27077753].

23. Elsheikh A, Phillips JR. Is scleral cross-linking a feasible treatment for myopia control? Ophthalmic Physiol Opt 2013; 33:385-9. [PMID: 23662971].

24. Brekelmans J, Goz A, Dickman MM, Brandis A, Sui X, Wagner HD, Nuijts RMMA, Scherz A, Marcovich AL. Corneal Stiffening by a Bacteriochlorophyll Derivative With Dextran and Near-Infrared Light: Effect of Shortening Irradiation Time up to 1 Minute. Cornea 2017; 36:1395-401. [PMID: 28644240].

25. Brekelmans J, Goz A, Dickman MM, Brandis A, Sui X, Wagner HD, Nuijts RMMA, Scherz A, Marcovich AL. Long-Term Biomechanical and Histologic Results of WST-D/NIR Corneal Stiffening in Rabbits, Up to 8 Months Follow-up. Invest Ophthalmol Vis Sci 2017; 58:4089-95. [PMID: 28828480].

26. Marcovich AL, Brandis A, Daphna O, Feine I, Pinkas I, Goldschmidt R, Kalchenko V, Berkutzki T, Wagner HD, Salomon Y, Scherz A. Stiffening of rabbit corneas by the bacteriochlorophyll derivative WST11 using near infrared light. Invest Ophthalmol Vis Sci 2012; 53:6378-88. [PMID: 22871842].

27. Mazor O, Brandis A, Plaks V, Neumark E, Rosenbach-Belkin V, Salomon Y, Scherz A. WST11, a novel water-soluble bacteriochlorophyll derivative; cellular uptake, pharmacokinetics, biodistribution and vascular-targeted photodynamic activity using melanoma tumors as a model. Photochem Photobiol 2005; 81:342-51. [PMID: 15623318].

28. Brandis A, Mazor O, Neumark E, Rosenbach-Belkin V, Salomon Y, Scherz A. Novel water-soluble bacteriochlorophyll derivatives for vascular-targeted photodynamic therapy: synthesis, solubility, phototoxicity and the effect of serum proteins. Photochem Photobiol 2005; 81:983-93. [PMID: 15839743].

29. Geraghty B, Jones SW, Rama P, Akhtar R, Elsheikh A. Age-related variations in the biomechanical properties of human sclera. J Mech Behav Biomed Mater 2012; 16:181-91. [PMID: 23182387].

30. Wollensak G, Iomdina E, Dittert DD, Salamatina O, Stoltenburg G. Cross-linking of scleral collagen in the rabbit using riboflavin and UVA. Acta Ophthalmol Scand 2005; 83:477-82. [PMID: 16029274].

31. Elsheikh A, Geraghty B, Alhasso D, Knappett J, Campanelli M, Rama P. Regional variation in the biomechanical properties of the human sclera. Exp Eye Res 2010; 90:624-33. [PMID: 20219460].

32. Boote C, Palko JR, Sorensen T, Mohammadvali A, Elsheikh A, Komáromy AM, Pan X, Liu J. Changes in posterior scleral collagen microstructure in canine eyes with an ADAMTS10 mutation. Mol Vis 2016; 22:503-17. [PMID: 27212875].

33. Pijanka JK, Abass A, Sorensen T, Elsheikh A, Boote C. A wide-angle X-ray fibre diffraction method for quantifying collagen orientation across large tissue areas: application to the human eyeball coat. J Appl Cryst 2013; 46:1481-9. .

34. Hayes S, White T, Boote C, Kamma-Lorger CS, Bell J, Sorenson T, Terrill N, Shebanova O, Meek KM. The structural response of the cornea to changes in stromal hydration. J R Soc Interface 2017; 14:20170062[PMID: 28592658].

35. Meek KM, Boote C. The use of X-ray scattering techniques to quantify the orientation and distribution of collagen in the corneal stroma. Prog Retin Eye Res 2009; 28:369-92. [PMID: 19577657].

36. Pijanka JK, Coudrillier B, Ziegler K, Sorensen T, Meek KM, Nguyen TD, Quigley HA, Boote C. Quantitative mapping of collagen fiber orientation in non-glaucoma and glaucoma posterior human sclerae. Invest Ophthalmol Vis Sci 2012; 53:5258-70. [PMID: 22786908].

37. Bell JS, Adio AO, Pitt A, Hayman L, Thorn CE, Shore AC, Whatmore JL, Winlove CP. Microstructure and mechanics of human resistance arteries. Am J Physiol Heart Circ Physiol 2016; 311:H1560-8. [PMID: 27663767].

38. Palero JA, de Bruijn HS, van der Ploeg van den Heuvel A, Sterenborg HJ, Gerritsen HC. Spectrally resolved multiphoton imaging of in vivo and excised mouse skin tissues. Biophys J 2007; 93:992-1007. [PMID: 17449667].

39. Raub CB, Suresh V, Krasieva T, Lyubovitsky J, Mih JD, Putnam AJ, Tromberg BJ, George SC. Noninvasive assessment of collagen gel microstructure and mechanics using multiphoton microscopy. Biophys J 2007; 92:2212-22. [PMID: 17172303].

40. Malik NS, Moss SJ, Ahmed N, Furth AJ, Wall RS, Meek KM. Ageing of the human corneal stroma: structural and biochemical changes. Biochim Biophys Acta 1992; 1138:222-8. [PMID: 1547284].

41. Campbell IC, Sherwood JM, Overby DR, Hannon BG, Read AT, Raykin J, Ethier CR. Quantification of Scleral Biomechanics and Collagen Fiber Alignment. Methods Mol Biol 2018; 1695:135-59. [PMID: 29190025].

42. Danford FL, Yan D, Dreier RA, Cahir TM, Girkin CA, Vande Geest JP. Differences in the region- and depth-dependent microstructural organization in normal versus glaucomatous human posterior sclerae. Invest Ophthalmol Vis Sci 2013; 54:7922-32. [PMID: 24204041].

43. Lau TY, Ambekar R, Toussaint KC. Quantification of collagen fiber organization using three-dimensional Fourier transform-second-harmonic generation imaging. Opt Express 2012; 20:21821-32. [PMID: 23037302].

44. Zyablitskaya M, Takaoka A, Munteanu EL, Nagasaki T, Trokel SL, Paik DC. Evaluation of Therapeutic Tissue Crosslinking (TXL) for Myopia Using Second Harmonic Generation Signal Microscopy in Rabbit Sclera. Invest Ophthalmol Vis Sci 2017; 58:21-9. [PMID: 28055099].

45. Winkler M, Jester B, Nien-Shy C, Massei S, Minckler DS, Jester JV, Brown DJ. High resolution three-dimensional reconstruction of the collagenous matrix of the human optic nerve head. Brain Res Bull 2010; 81:339-48. [PMID: 19524027].

46. Zyablitskaya M, Takaoka A, Munteanu EL, Nagasaki T, Trokel SL, Paik DC. Evaluation of Therapeutic Tissue Crosslinking (TXL) for Myopia Using Second Harmonic Generation Signal Microscopy in Rabbit Sclera. Invest Ophthalmol Vis Sci 2017; 58:21-9. [PMID: 28055099].

47. Nguyen C, Midgett D, Kimball EC, Steinhart MR, Nguyen TD, Pease ME, Oglesby EN, Jefferys JL, Quigley HA. Measuring Deformation in the Mouse Optic Nerve Head and Peripapillary Sclera. Invest Ophthalmol Vis Sci 2017; 58:721-33. [PMID: 28146237].

48. Green EM, Mansfield JC, Bell JS, Winlove CP. The structure and micromechanics of elastic tissue. Interface Focus 2014; 4:20130058[PMID: 24748954].

49. Steven P, Hovakimyan M, Guthoff RF, Hüttmann G, Stachs O. Imaging corneal crosslinking by autofluorescence 2-photon microscopy, second harmonic generation, and fluorescence lifetime measurements. J Cataract Refract Surg 2010; 36:2150-9. [PMID: 21111320].

50. Merna N, Robertson C, La A, George SC. Optical imaging predicts mechanical properties during decellularization of cardiac tissue. Tissue Eng Part C Methods 2013; 19:802-9. [PMID: 23469868].

51. Steven P, Hovakimyan M, Guthoff RF, Hüttmann G, Stachs O. Imaging corneal crosslinking by autofluorescence 2-photon microscopy, second harmonic generation, and fluorescence lifetime measurements. J Cataract Refract Surg 2010; 36:2150-9. [PMID: 21111320].

52. Theodossiou T, Rapti GS, Hovhannisyan V, Georgiou E, Politopoulos K, Yova D. Thermally induced irreversible conformational changes in collagen probed by optical second harmonic generation and laser-induced fluorescence. Lasers Med Sci 2002; 17:34-41. [PMID: 11845366].

53. Zoumi A, Yeh A, Tromberg BJ. Imaging cells and extracellular matrix in vivo by using second-harmonic generation and two-photon excited fluorescence. Proc Natl Acad Sci U S A 2002; 99:11014-9. [PMID: 12177437].

54. Baldwin AK, Simpson A, Steer R, Cain SA, Kielty CM. Elastic fibres in health and disease. Expert Rev Mol Med 2013; 15:e8[PMID: 23962539].

55. Lewis PN, White TL, Young RD, Bell JS, Winlove CP, Meek KM. Three-dimensional arrangement of elastic fibers in the human corneal stroma. Exp Eye Res 2016; 146:43-53. [PMID: 26704458].

56. White TL, Lewis PN, Young RD, Kitazawa K, Inatomi T, Kinoshita S, Meek KM. Elastic microfibril distribution in the cornea: Differences between normal and keratoconic stroma. Exp Eye Res 2017; 159:40-8. [PMID: 28315339].

57. White TL, Lewis P, Hayes S, Fergusson J, Bell J, Farinha L, White NS, Pereira LV, Meek KM. The Structural Role of Elastic Fibers in the Cornea Investigated Using a Mouse Model for Marfan Syndrome. Invest Ophthalmol Vis Sci 2017; 58:2106-16. [PMID: 28395026].

58. Sell DR, Monnier VM. Isolation, purification and partial characterization of novel fluorophores from aging human

insoluble collagen-rich tissue. Connect Tissue Res 1989; 19:77-92. [PMID: 2791558].

59. Liu K, Sun J, Song Y-G, Liu B, Xu Y-K, Zhang S-X, Tian Q, Liu Y. Superoxide, Hydrogen Peroxide and Hydroxyl Radical in D1/D2/cytochrome b-559 Photosystem II Reaction Center Complex. Photosynth Res 2004; 81:41-7. [PMID: 16328846].

60. Meek KM, Knupp C. Corneal structure and transparency. Prog Retin Eye Res 2015; 49:1-16. [PMID: 26145225].

61. Brinckmann J, Neess CM, Gaber Y, Sobhi H, Notbohm H, Hunzelmann N, Fietzek PP, Müller PK, Risteli J, Gebker R, Scharffetter-Kochanek K. Different pattern of collagen cross-links in two sclerotic skin diseases: lipodermatosclerosis and circumscribed scleroderma. J Invest Dermatol 2001; 117:269-73. [PMID: 11511304].

62. Ricard-Blum S, Bresson-Hadni S, Vuitton DA, Ville G, Grimaud JA. Hydroxypyridinium collagen cross-links in human liver fibrosis: study of alveolar echinococcosis. Hepatology 1992; 15:599-602. [PMID: 1312984].

63. van der Slot-Verhoeven AJ, van Dura EA, Attema J, Blauw B, Degroot J, Huizinga TW, Zuurmond AM, Bank RA. The type of collagen cross-link determines the reversibility of experimental skin fibrosis. Biochim Biophys Acta 2005; 1740:60-7. [PMID: 15878742].

64. Hayes S, Aldahlawi N, Marcovich AL, Brekelmans J, Goz A, Scherz A, Young RD, Bell JS, O'Brart DP, Nuijts RMMA, Meek KM. The effect of bacteriochlorophyll derivative WST-D and near infrared light on the molecular and fibrillar architecture of the corneal stroma. Sci Rep 2020; 10:9836-[PMID: 32555309].

65. Malik NS, Meek KM. Vitamins and analgesics in the prevention of collagen ageing. Age Ageing 1996; 25:279-84. [PMID: 8831872].

66. Tanaka S, Avigad G, Brodsky B, Eikenberry EF. Glycation induces expansion of the molecular packing of collagen. J Mol Biol 1988; 203:495-505. [PMID: 3143838].

67. Fullwood NJ, Meek KM. A synchroton X-ray study of the changes occurring in the corneal stroma during processing for electron microscopy. J Microsc 1993; 169:53-60. [PMID: 8445631].

68. Hayes S, Kamma-Lorger CS, Boote C, Young RD, Quantock AJ, Rost A, Khatib Y, Harris J, Yagi N, Terrill N, Meek KM. The effect of riboflavin/UVA collagen cross-linking therapy on the structure and hydrodynamic behaviour of the ungulate and rabbit corneal stroma. PLoS One 2013; 8:e52860[PMID: 23349690].

69. Abass A, Hayes S, White N, Sorensen T, Meek KM. Transverse depth-dependent changes in corneal collagen lamellar orientation and distribution. J R Soc Interface 2015; 12:20140717[PMID: 25631562].

70. Zhang Y, Zhang W, Snow T, Ju Y, Liu Y, Smith AJ, Prabakar S. Minimising chemical crosslinking for stabilising collagen in acellular bovine pericardium: Mechanistic insights via structural characterisations. Acta Biomater 2022; 152:113-23. [PMID: 36049624].

71. Hirst GS, Sarker S, Terry BS. Differences in the mechanical properties of intestinal tissue based on preservation freezing duration and temperature. J Mech Behav Biomed Mater 2024; 152:106440[PMID: 38340478].

72. Zyablitskaya M, Munteanu EL, Nagasaki T, Paik DC. Second Harmonic Generation Signals in Rabbit Sclera As a Tool for Evaluation of Therapeutic Tissue Cross-linking (TXL) for Myopia. J Vis Exp 2018; 131:56385-[PMID: 29364259].

73. Jan NJ, Sigal IA. Collagen fiber recruitment: A microstructural basis for the nonlinear response of the posterior pole of the eye to increases in intraocular pressure. Acta Biomater 2018; 72:295-305. [PMID: 29574185].

74. McQuaid R, Li J, Cummings A, Mrochen M, Vohnsen B. Second-harmonic reflection imaging of normal and accelerated corneal crosslinking using porcine corneas and the role of intraocular pressure. Cornea 2014; 33:125-30. [PMID: 24322797].

75. Miao Y, Liu J, Akella SS, Wang J, Li S, Chuck RS, Zhang C. Changes in Rat Scleral Collagen Structure Induced by UVA-Riboflavin Crosslinking at Various Tissue Depths in Whole Globe Versus Scleral Patch. Transl Vis Sci Technol 2022; 11:2-[PMID: 35913416].

76. Bueno JM, Gualda EJ, Giakoumaki A, Pérez-Merino P, Marcos S, Artal P. Multiphoton microscopy of ex vivo corneas after collagen cross-linking. Invest Ophthalmol Vis Sci 2011; 52:5325-31. [PMID: 21467175].

77. Diakonis VF, Likht NY, Yesilirmak N, Delgado D, Karatapanis AE, Yesilirmak Y, Fraker C, Yoo SH, Ziebarth NM. Corneal elasticity after oxygen enriched high intensity corneal cross linking assessed using atomic force microscopy. Exp Eye Res 2016; 153:51-5. [PMID: 27725199].

78. Wang M, Zhang F, Liu K, Zhao X. Safety evaluation of rabbit eyes on scleral collagen cross-linking by riboflavin and ultraviolet A. Clin Exp Ophthalmol 2015; 43:156-63. [PMID: 25070292].

79. Hoang QV, Dutta S, McFadden SA, Mamou J. Biomechanical Properties Change in the Peri-Equatorial Region in Myopic Guinea Pig Sclera: Insights Toward Location of Early Changes During Myopization. Invest Ophthalmol Vis Sci 2024; 65:3846-.

80. Zhang X, El Hamdaoui M, Lim S, Grytz R, Weickenmeier J. Microindentation reveals softening of the equatorial and anterior sclera during early myopia development in tree shrew eyes. Acta Biomater 2025; 201:446-56. [PMID: 40518097].

81. Goz A. Structural and Biomechanical Effects of Bacteriochlorophyll Derivatives (BchlDs) and near Infrared Light (NIR) on Sclera: Elucidating the Mechanism of Action [Ph.D.]. Israel: The Weizmann Institute of Science (Israel); 2019.

82. Vogels DHJ, Abdulla Y, Myles W, Cummings S, Agemy L, Yechezkel T, Marcovich AL, Scherz A, LaPointe VLS, McFadden SA, Dickman MM. A transpupillary approach for crosslinking Guinea pig sclera using WST11 and near-infrared light. Sci Rep 2026; 16:6098-[PMID: 41577952].